PROCEEDINGS, 45th Workshop on Geothermal Reservoir Engineering
Stanford University, Stanford, California, February 9-11, 2020
SGP-TR-212

SAND2020-0711C

Thermal expansion, fluid flow, and thermal shock of cement and a cement/steel interface at elevated pressure and temperature

Stephen J. Bauer[1], Perry Barrow, Tatiana Pyatina[2], Toshifumi Sugama[2]

[1]GSandia National Laboratories, Albuquerque, NM, 87185

[2]Brookhaven National Lab, Upton, NY

sjbauer@sandia.gov[1]; pbarrow@sandia.gov[1]; tpyatina@bnl.gov[2]; tsugama@bnl.gov[2];

Keywords: cement, thermal expansion, fluid flow, high temperature, high pressure

ABSTRACT

A critical parameter for the well integrity in geothermal storage and production wells subjected to frequent thermal cycling is the interface between metal casing and cement composite. A team from Sandia and Brookhaven National Labs is evaluating Thermal Shock-Resistant Cement (TSRC) to facilitate its use during severe and repeated thermal cycling in geothermal wells. For this portion of the laboratory study we report on preliminary results from subjecting TSRC to high temperature (T> 200°C), at a confining pressure of 13.8 MPa, and pore water pressure of 10.4 MPa and to heat cycling tests (250°C heat – 18°C water). Our work includes developing the test system to measure dimensional changes during heating and cooling and fluid flow at elevated temperature and pressure. We studied three sample types; steel, solid cement and a steel cylinder sheathed with cement. In the latter sample type, we flowed water through the inside of the steel cylinder rapidly to develop an inner to outer thermal gradient on this test geometry. Comparison of TSRC and common ordinary Portland Cement (OPC)-based formulations in heat-water cycles showed cement- carbon steel (CS) bond to be the weak point for both systems with OPC-CS bond strength decrease of 84% and TSRC-CS bond decrease of 11% after 20 cycles. The better TSRC performance could not be explained by the difference in cements coefficients of thermal expansion but was shown to be, at least partially, the result of differences in their interfacial chemistries.

1. INTRODUCTION

In Reservoir Thermal Energy Storage (RTES) systems the storage medium is at elevated pressures and temperatures of up to 300°C. The reservoir rocks and sands containing hot geo-steam and geo-fluids, and confined hot aquifer located above bedrock heated by magma, may provide a flexible source of energy for electricity generation on demand. Cold water is injected underground through an injection well and hot steam/water is recovered through a production well and used to generate electricity. The cold condensate is returned underground for makeup water heat recovery through the injection well. In RTES, repeated thermal shock (TS) conditions experienced by casing-cement sheaths is the major concern for the integrity of the wells. At the beginning of electricity generation, the near-the-surface, relatively cool cement sheath in the production well suffers from TS from hot geo-fluid, while the hot cement sheath deep in the injection well encounters TS with the sudden drop in temperature of >160°C as cold water passes through the casing. Furthermore, when electricity is no longer required, the cooled injection casing heats up to hot RTES temperatures. In contrast, hot production casing cools off. Thus, during frequent thermal cycles in injection and production wells, the cement sheath repeatedly undergoes thermal stresses by thermal expansion (microcrack development in sheath by compressive stress) and contraction of casing (micro-annulus development between the sheath and casing by tensile stress). Our work scope for the project involves study of steel, TSR cement and the interface of these materials in the form of a TSR cement sheathed pipe.

This paper evaluates Thermal Shock-Resistant Cement (TSRC) developed by Brookhaven National Laboratory (BNL)[1]. Our work focused on thermal expansion, and fluid flow through the TSRC, and the application of thermal shock to a steel/TSRC sheathed sample. The key contributions of this work to the geothermal community are (1) development of a test system to make measurements at elevated temperature and pressure, (2) Measurements of thermal expansion and fluid flow of TSRC at elevated temperature and pressure conditions relevant to in situ geothermal conditions, (3) development of a test system to thermally shock a steel/TSRC sheathed sample at elevated temperature and pressure conditions relevant to in situ geothermal conditions and, (4) evaluation of comparative performance of TSRC and common high-temperature ordinary Portland Cement (OPC)-based sheath samples under conditions of dry heat thermal shock at ambient pressures.

The testing program included measurements on a steel cylinder, a cylinder of TSRC, and a TSR cement sheathed pipe. It was planned to measure thermal expansion of the steel at pressure, thermal expansion of the water-saturated TSRC at and pore water pressure, fluid flow through the TSRC at elevated temperature and pore water pressure, and lastly to thermally shock water-saturated TSR cement sheathed pipe while at elevated pressure and temperature. The sheathed samples were subjected to a few cycles due to long durations of test (weeks).

Sandia National Laboratories is a multimission laboratory managed and operated by National Technology & Engineering Solutions of Sandia, LLC, a wholly owned subsidiary of Honeywell International Inc., for the U.S. Department of Energy's National Nuclear Security Administration under contract DE-NA0003525.

2. EXPERIMENTAL

2.1 Samples Tested and Laboratory Setup

Three samples were evaluated in this test series, a hollow cylinder of carbon steel, a solid TSR cement sample, and a steel tube with a sheath of cement around it. . TSR Cement is a special formulation calcium-aluminate cement blend with fly ash, type F and sodium meta-silicate activator, prepared by Brookhaven National Laboratory. The cement formulations, compositions, and suppliers of the starting materials can be found elsewhere[2]. Micro carbon fibers were used at 6% by weight of blend in both formulations to improve the compressive toughness, and suppress and control the cracks width and propagation as described in [2], [3]. Dyckerhoff, type North, oil field, class G cement was used to prepare OPC/SiO_2 blend. The steel was cut to length and end ground perpendicular to length, the latter two samples were ground round on a wet lathe and then end ground perpendicular to length in a water bath. The cement and the cement sheathed steel samples were always stored in water prior to jacketing. Sample dimensions are given in Table 1, and images of the cement and cement sheathed steel are shown in Figure 1. Air bubbles were visible in the cement and some discontinuous cracks.

Table 1. Sample Dimensions

	Steel	**Cement**	**Cement Sheathed Steel**
Diameter (OD cm)	7.0	6.8	6.5
Diameter (ID cm)	4.4	0.0	2.2
Area (cm^2)	5.2	36.3	14.2
Length (cm)	17.8	17.0	17.4
Mass (g)	3213.1	1162.4	1048.0

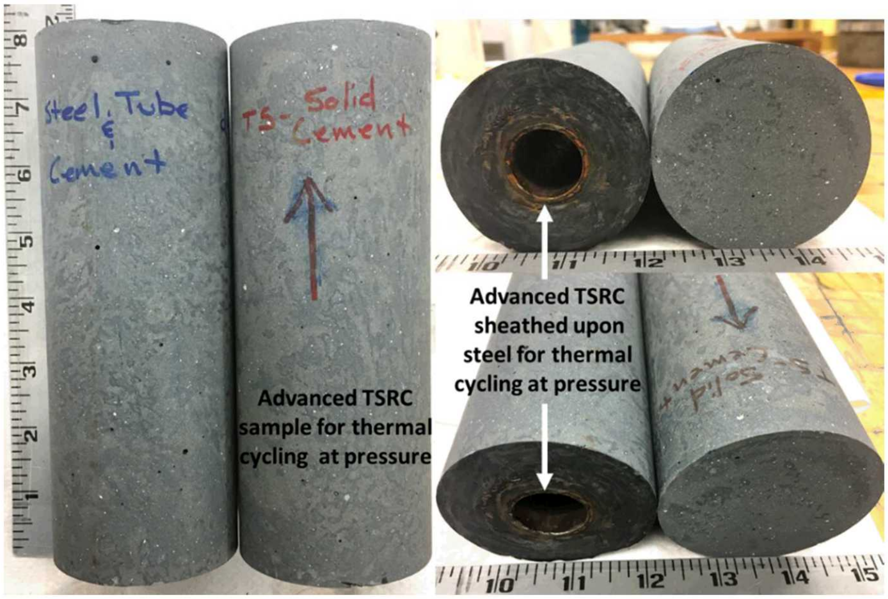

Figure 1: Images of TSR cement and TSR cement sheathed pipe considered in this study.

To support understanding of material behavior of each sample at elevated temperature and pressure we have developed a laboratory-based test system which allows for high temperature sample displacement to determine strain, fluid flow through cement and fluid flow at high rates. The first measure allows us to estimate the thermal coefficient, the second allows us to estimate permeability, and the third allows us to create thermal gradients quickly in such a manner as to thermally shock the sample at elevated temperatures and pressure.

2.2 Test System

An experimental test system was developed which can be used to simulate reasonable downhole geothermal environmental conditions. It is capable of subjecting jacketed cement specimens to high temperature, elevated confining pressure and differential stresses, and high pore-water pressures. Test conditions of 13.8 MPa confining pressure, 1.5 MPa differential stress, and 10.4 MPa pore water pressure were chosen as representative for this initial study; all tests were initialized to these conditions. The intent was to conduct the tests with no differential stress, however, the test system requires a small axial load, we chose 1.5 MPa. The 10.4 MPa pore water pressure was the average; upstream and downstream pressures are varied to create flow through the specimen.

The test temperature ranged from 25°C to 220°C and was increased and decreased in approximately 50°C increments. Temperature estimates during the experiments are made at the (1) outer vessel top, (2) outer vessel middle, (3) inside the vessel in the confining fluid (4) on the pore fluid tube entering the pressure vessel, and (5) on the pore fluid tube exiting the pressure vessel. Test system temperature is monitored using (1), (2), (3) during heating and cooling and we use these temperatures to determine the sample temperature. Test temperatures in this paper are confining fluid temperature.

The test system needed to be able to achieve the test conditions and to maintain these conditions for extended times (weeks to months). This long test condition time was needed because we have limited samples, the test system was time consuming and laborious to set-up, achieve temperature, pressure, and stress conditions, and to conduct the tests. And, consequently, we desired to obtain as much data as possible from an individual sample.

We used an in-house built creep test system (Figure 2) already capable of maintaining the above temperature, stress, and pressure conditions, with recently added flow through pore pressure capability. The test system is controlled with a computer-based interfaced system and simultaneously controls the test and acquires test data at user specified time-based intervals. Data collection rates are high (1 sec) for test active testing and low (1 min) for quiescent times.

The testing system consists of a sample assembly (Figure 2A), a reaction frame (Figure 2B) that generates the axial force by reacting against a hydraulic cylinder located at the base of the frame, and a pressure vessel that houses specimens during testing. The reaction frame system can apply loads of up to 450 kN. The pressure vessel (Figure 2D) is rated to 70 MPa and is equipped with electrical band heaters capable of maintaining test temperatures up to approximately 250°C. Silicon oil is used as the confining medium. Fluid confining pressures are coarsely adjusted using an air-assisted pump and finely adjusted and maintained constant using a syringe pump (Figure 2E) that either injects or withdraws silicon oil from the vessel. Vessel pressures are measured by a pressure transducer plumbed into the hydraulic line leading from the vessel to the syringe pump. Axial loads applied by the hydraulic cylinder are measured by a load cell located directly above the cylinder in line with the axial push-rod that extends into the pressure vessel and applies axial load to the ends of the specimen. Test temperature is recorded by three thermocouples, one located near the top of the pressure vessel, one near the vessel midheight, and one inside the pressure vessel. Pore-water temperatures are measured using thermocouples strapped to the high-pressure tubing leading into and out of the pressure vessel.

Pore fluid pressures (using tap water as the permeant) are created using two opposing ISCO pumps (maximum pressure 25.9 MPa) plumbed into the top and bottom of the sample (Figure 2C).

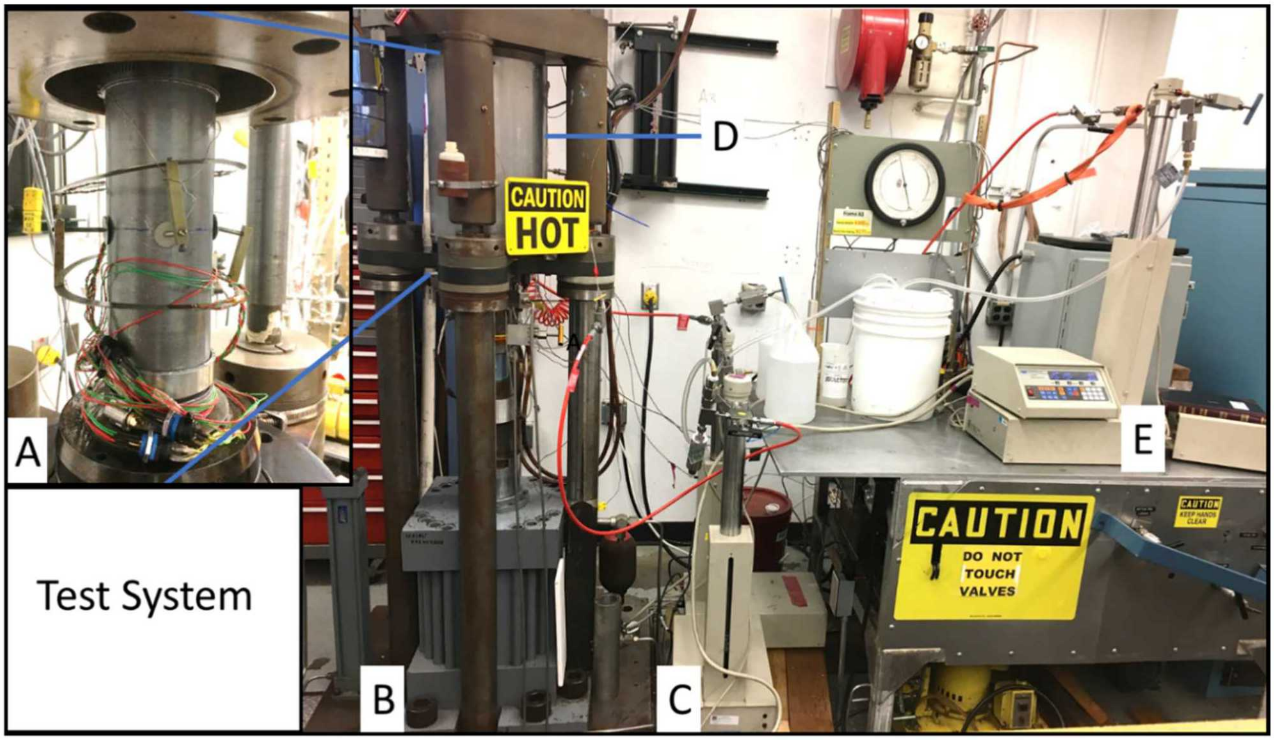

Figure 2: Test system. A: Assembled specimen prior to lowering the pressure vessel; B: Loading frame; C: Pore pressure generating syringe pumps; D: Pressure vessel encased in insulated heating furnace; E: Confining fluid controlling syringe pump.

2.3 Sample Assembly

The test specimen for this study is a right-circular-cylinder of steel, TSR Cement, and steel sheathed with TSR CementThe sample (not visible), was kept in a water bath except when being end prepped. The nippled coupling connects the sample to the pore fluid pumping system at the top and bottom, and the O-rings isolate it from the confining fluid (Figure 3). A metal mesh pad is placed on opposing ends of the sample between the cement and end cap. The sample is jacketed in a lead sleeve and sealed to the end caps with silicon O-rings and knife edge metal-metal seals. During the sealing process the lead jacket is pressed firmly against the knife edge, forming the metal-metal seals with ~4 to 7 MPa gas pressure. Sample displacements are measured using external displacement transducers for axial displacements (LVDTs) and a pair of high temperature clip-on gages[4] for lateral displacements (Figure 3). The Schuler gages are self-temperature compensating by nature of full bridge wiring configuration.

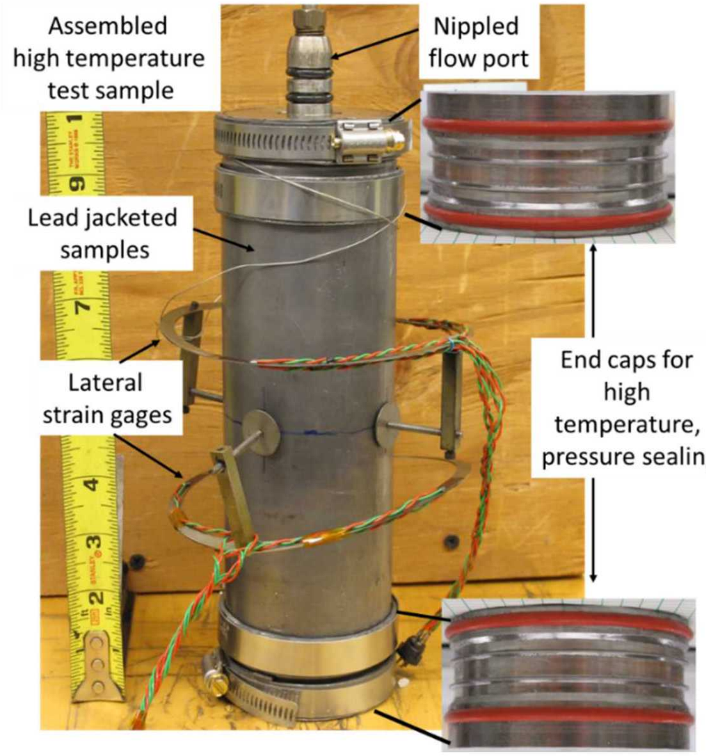

Figure 3: Assembled high temperature test sample showing specially designed high temperature end caps, lead jacketing, lateral strain gages and nippled flow ports.

Data collected in the experimental study included force, pressure, temperature, displacements, and volume change of water versus time. Typically, these data are acquired using electronic transducers in which the electrical output is proportional to the change in the measured variable. In all cases, the constants of proportionality were determined through calibration using standards traceable to the National Institute for Standards and Technology.

2.4 Test Conduct

Once in the pressure vessel, the sample is subjected to the small axial stress (1-1.5 MPa). The axial differential stress is maintained during application of confining pressure. After about 4 MPa confining pressure is applied, pore water pressure is introduced to the sample. Then confining and pore pressures are together increased to test conditions of 13.8 and 10.4 MPa, respectively, resulting in an effective pressure of ~ 3.5 MPa. Confining pressure is held constant at 13.8 MPa for the duration of the test. Once at these pressure conditions, temperature is ramped up and down to ~200°C in 50°C or 100°C increments and held for varying amounts of time. The 3.5 to 4 MPa effective confining pressure upon the soft lead effectively seals the jacket against the sample especially as temperatures are increased. During the hold periods we circulated water through the sample by increasing the upstream pressure and decreasing the downstream pressure by ~0.345 MPa and measuring flow. For the steel sample tests, no water was moved through the sample at temperature.

The steel specimen was heated and cooled, and its dimensional change recorded. The steel was subjected to three 180-hour heating and cooling cycles. From this heating and cooling, thermal expansion of the cylinder at 13.8 MPa confining pressure was estimated.

The water-saturated cement specimen was heated and cooled, held at specific temperatures, and its dimensional change recorded. At specific temperatures, an upstream pressure increase coincides with a downstream pressure decrease of ~0.345 MPa. The pumps reacted with water flow which continued for a few hours, depending on the flow rate. This flow measurement allowed for permeability of the cement to be estimated.

The water-saturated cement sheathed steel specimen was heated to specific temperatures and after thermal equilibration was reached, room temperature water was rapidly flowed through the inner tubing. Temperature gradients of +100°C were attained in 4 to 5 minutes. This created our attempt at a thermal shock to the inner portion of the sample.

In the dry thermal shock experiments bulk or sheath cement samples were subjected to repeated 250°C autoclaving (hydrothermal conditions, 3.9 MPa) followed by 4 hrs at 250°C dry heat and 15 min 18°C cold water exposure directly after the heat by cold water passing through the tubes (100 ml/s) (Figure 4) or by submerging bulk samples into cold water. Although the dry conditions could be expected only in hot rock formations, this set up reproduces both compressive stress (during the heat) and tensile stress (during the cold water going through the casing tube) of cement and is relevant for the combined solar-geothermal heat recovery-storage where very high temperatures are reached during solar heating. Furthermore, the heat conditions expose cement to carbon dioxide commonly present in geothermal wells and causing cement carbonation, which is similar under dry heat and hydrothermal conditions. Finally, the advantage of severe conditions is acceleration of cement damage allowing identification of critical parameters for its stability and degradation in a relatively short time.

Coefficient of Thermal Expansion (CTE) measurements followed ASTM C531-00. Calculations of CTE assumed that hydrating cement is a new material after each cycle because of the on-going composition changes. The measured values of the bar length were compared against its cold length value at each cycle and not to the original length of the bar. For more details see[5].

The dry-heat thermal shock conditions were modeled by two types of initial heat exposure after the 24hrs of hydrothermal curing at 250°C. In the first set up the temperature was ramped up to 250°C (10°C/min temperature increase rate) and the samples stayed at that temperature overnight (10 cycles). In the second set up the samples were initially heated to 60°C for 2 days before the thermal cycling and then exposed to 250°C (5°C/min temperature increase rate) for 4 hrs in each cycle before cold water exposure (20 cycles). Fast high-temperature heating causes cement shrinkage and damage of the cement-metal bond, allowing for accelerated testing of the potential damage. On the other hand, such conditions are not likely in geothermal wells where the temperature increase is usually very gradual and may happen over several days after the cement placement. The second set up used in the testing modeled slower heating of cement samples with lower shrinkage.

The data analyses for the control samples after fast-heating high-temperature exposure and slow heating showed that there was no significant difference in phase compositions and morphologies of TSRC samples prepared with two different initial heating schedules, however, the mechanical properties of the samples differed significantly.

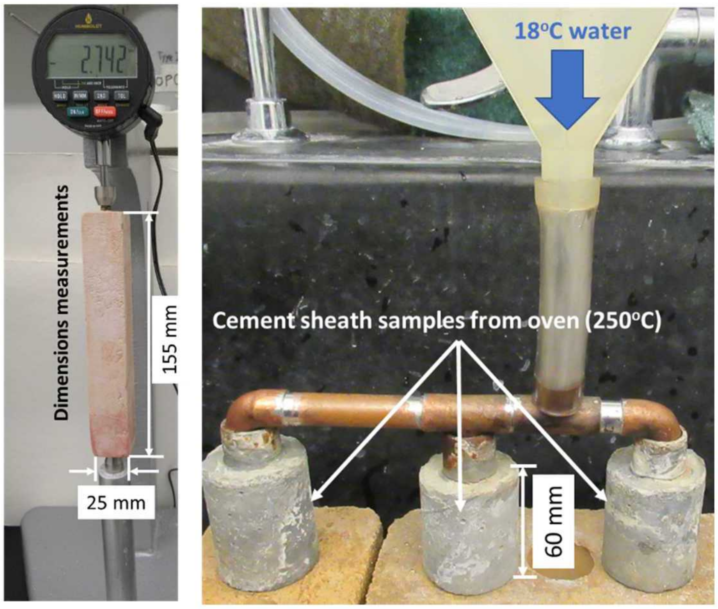

Figure 4. Set ups for CTE measurements and thermal shock of heated samples

3. RESULTS AND DISCUSSION

3.1 Steel

The steel was cycled to ~220°C three times, each cycle lasting about 180 hours, the first two times in steps, and the 3rd time in a single step to the maximum temperature; steel testing lasted about four weeks. An example of the heating and cooling is given in Figure 5. The sample, once pressurized, was heated in four steps, with a hold at each temperature. Displacement measurements on the sample are averaged to calculate strains and thermal expansion coefficient as a function of temperature.

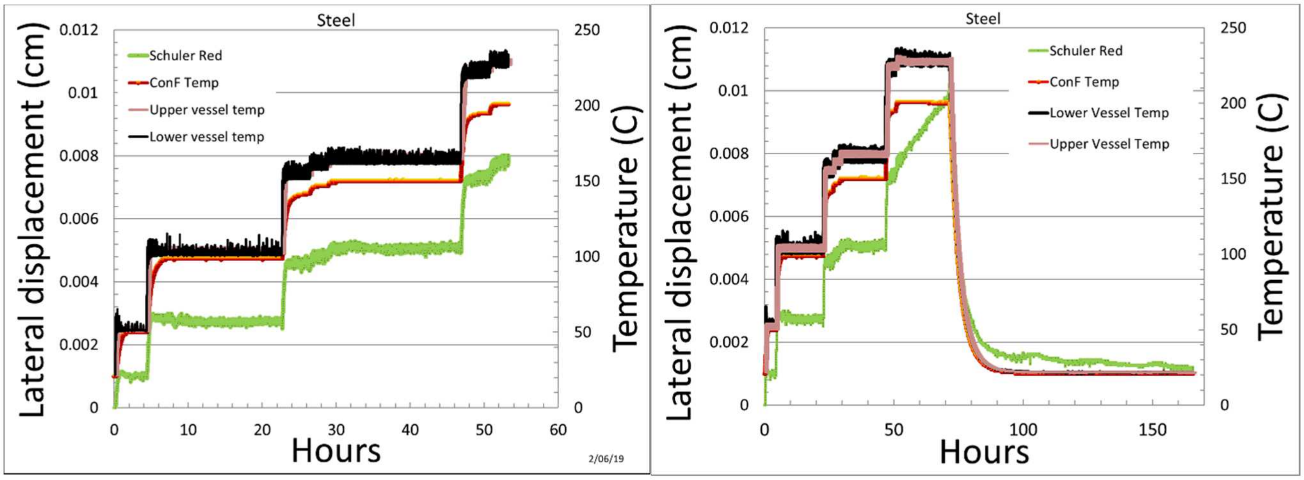

Figure 5. Displacement and temperature records for first and second heating cycles for steel.

3.2. Cement

The cement sample, after being subjected to 13.8 MPa confining pressure and 10.3 MPa pore pressure was subjected to thermal cycling and flow tests over the course of 16 days. Each work day the sample was heated or cooled to a test temperature, water flowed through it, and then the sample was sometimes cooled to reduce the high temperature exposure on the equipment. An example of sample heating and cooling, and its expansion and compaction is given in Figure 6. Also shown are the flow periods for these tests. To estimate flow rates, the volume in the pumps are recorded at the start and the end of the flow, giving an average flow rate to later estimate permeability.

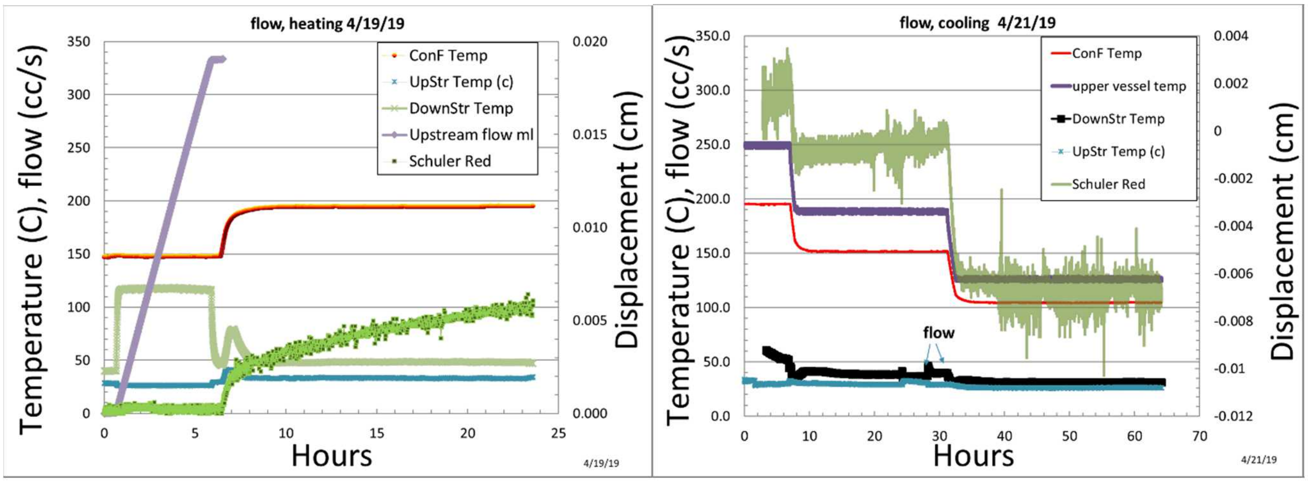

Figure 6. Examples of cooling temperature cycle, displacements, and flow period for cement sample. Confining fluid temperature, upstream and downstream temperature, fluid flow and sample displacements are plotted versus test time.

Thermal expansion is calculated as the strain per °C for heating and cooling cycles, the reported values are determined by dividing sample strain by the temperature change in the cycles. Permeability estimates are made from the water flow measurements. Thermal expansion and permeability estimates are given in Table 2. Permeability calculated using Darcy's law is expressed as the measured flow rate of fluid crossing a unit area and is proportional to the pressure differential measured across the ends of the specimen. The flow rate q and permeability k are related by the following equation:

$$q = \frac{k}{\mu} A \left(\frac{\Delta p}{L}\right) \tag{1}$$

where q, k, μ, A, L, Δp are volumetric fluid flow rate, absolute permeability, fluid viscosity, cross-sectional area, length and pressure drop over the length L, respectively.

Table 2. Date, temperature, flow rate, water viscosity, permeability, cement and steel CTE

Date	Confining Fluid T(°C)	Flow rate (cc/s)	Viscosity (cp)	Permeability (μD)	Cement CTE (°C^{-1})	Steel CTE (°C^{-1})
3/11/2019	50				3.2E-05	
3/12/2019	50				5.3E-05	4.4E-05
3/13/2019	53.1	0.007	0.55	0.21	4.1E-06	
3/15/2019	50.2	0.007	0.55	0.21	9.6E-06	
3/18/2019	102	0.014	0.28	0.23	3.0E-05	2.9E-05
3/19/2019	148	0.018	0.18	0.19	4.1E-06	
3/20/2019	195	0.003	0.14	0.02	4.0E-06	
3/21/2019	152	0.001	0.18	0.01	4.4E-05	
3/25/2019	104	0.0031	0.27	0.05	2.2E-05	
3/25/2019	104	0.0035	0.27	0.05	4.9E-05	
3/26/2019	151	0.008	0.18	0.09	3.2E-05	2.8E-05
3/26/2019	151	0.012	0.18	0.13	5.3E-05	
3/27/2019	151	0.009	0.18	0.09	4.1E-06	
3/28/2019	197	0.014	0.14	0.11	9.6E-06	3.3E-05
3/28/2019	196	0.017	0.14	0.14	3.2E-05	
Average				0.12	2.5E-05	3.4E-05

The CTE of the steel at 13.8MPa confining pressure varies slightly and estimated to be approximately 2 to 5 x 10^{-5}/°C, over this temperature range (Table 2). The CTE of steel should not be affected by pressure, and the thermal expansion of steel should be constant for this temperature range. The reported CTE of carbon steel is 1.2 E-05 °C^{-1} and is 1.8 E-05 °C^{-1} for stainless steel (1). We attribute our variability to measurement accuracy and instrument drift.

The CTE of the cement, while water saturated at ~3 MPa effective confining pressure, is in the range of 1 to 5 x 10^{-5}/°C over this temperature range (Table 2), with some variability.

Water viscosity is temperature-dependent (Figure 7) and we use it and equation 1 to calculate the fluid flow rate variation in a non-temperature dependent permeability material (Figure 7) with a permeability of 0.1 μD. Because water viscosity decreases with increasing temperature, flow rate would be expected to increase (with all else being equal in equation 1).

The average fluid flow rates from the measurements (Figure 8) shows an increase with increasing temperature and they trend similarly to the non-temperature dependent permeability material (K= 0.1 μD). This implies that the permeability of the cement may only be slightly temperature dependent. We measure a slight decrease in permeability of the cement with increasing temperature. If true, this could be explained by pore and crack closure with increasing temperature of the confined cement.

---

[1] Obtained from https://www.engineeringtoolbox.com/pipes-temperature-expansion-coefficients

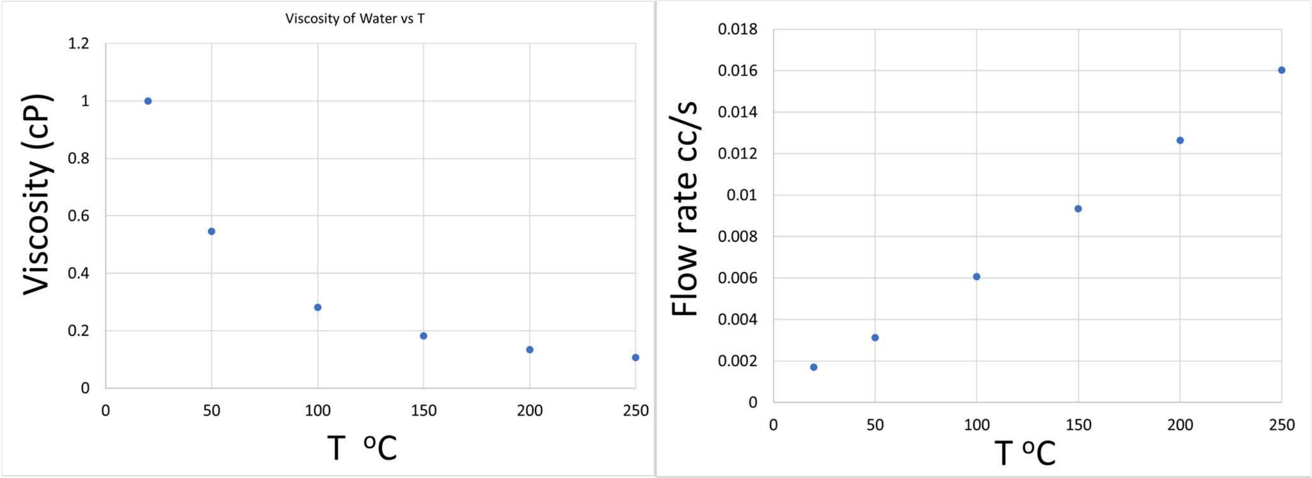

Figure 7. Viscosity of water versus temperature 2 **(left) and flow rate (right) change for a 0.1 µD material considering viscosity of water change with increasing temperature.**

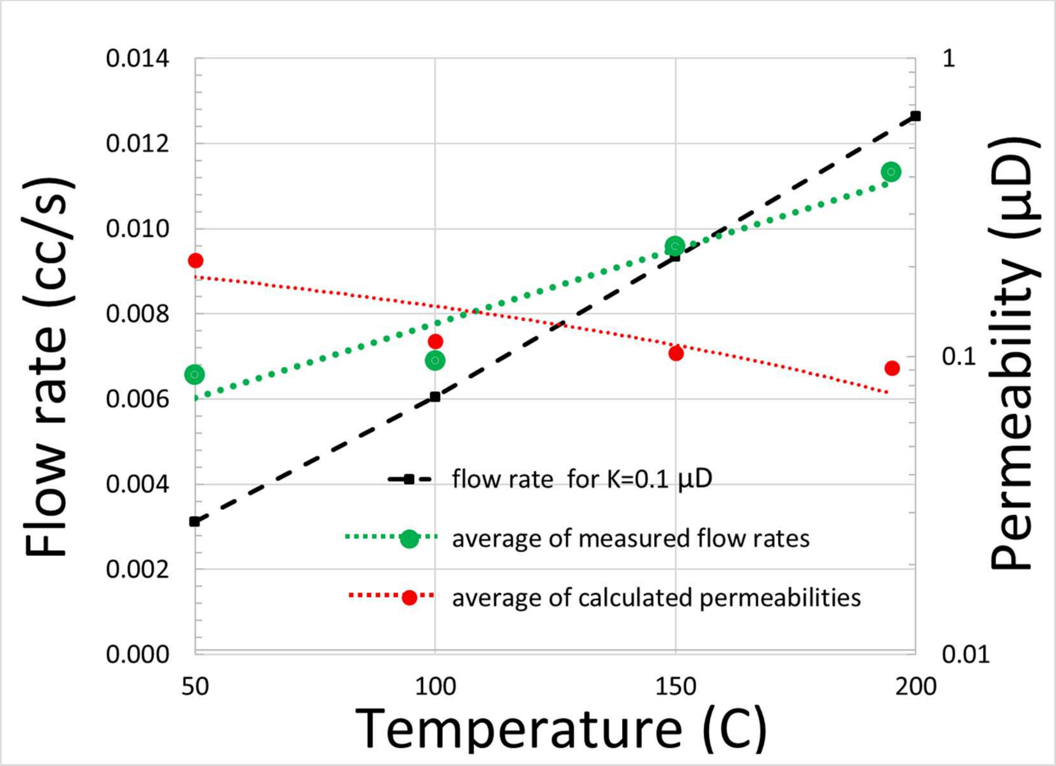

Figure 8. Average of measured flow rates, average of calculated permeabilities and flow rate change for a 0.1 µD material considering temperature dependent water viscosity.

---

[2] https://www.steamtablesonline.com

3.3 Cement sheathed steel

The primary purpose of this test configuration is to thermally shock the steel-cement interface. This was achieved by flowing chilled water into the inner sample tubing at high flow rates. Early in the testing we flowed at 20-40 cc/min, and later we were able to increase the flow rate to 100 cc/min. The limits of the flow were the size of the reservoir (500 cc), the tubing orifice temperature in the high-pressure tubing, and the chilling of the return water into the receiving pump. Using ice baths for the inlet water and exiting water, we were able to achieve approximately a 100°C decrease in the core temperature of the water (and thus steel), and with the outer portion of the cement at +200°C, a significant gradient was developed in 5 minutes of flow. A 25-hour test period is shown in Figure 9 (left), and an expanded time scale of one hour is shown in Figure 9 (right).

In Figure 10, the Schuler gage displacement data is added to the plot. It appears that during the flow and quiescent periods, the sample expands. The details of the thermally driven behavior are complex during the flow, suggesting some complex interactions between the components.

The single sample was subjected to approximately twelve thermal shock cycles over the course of eight days. The test was terminated because of a jacket leak.

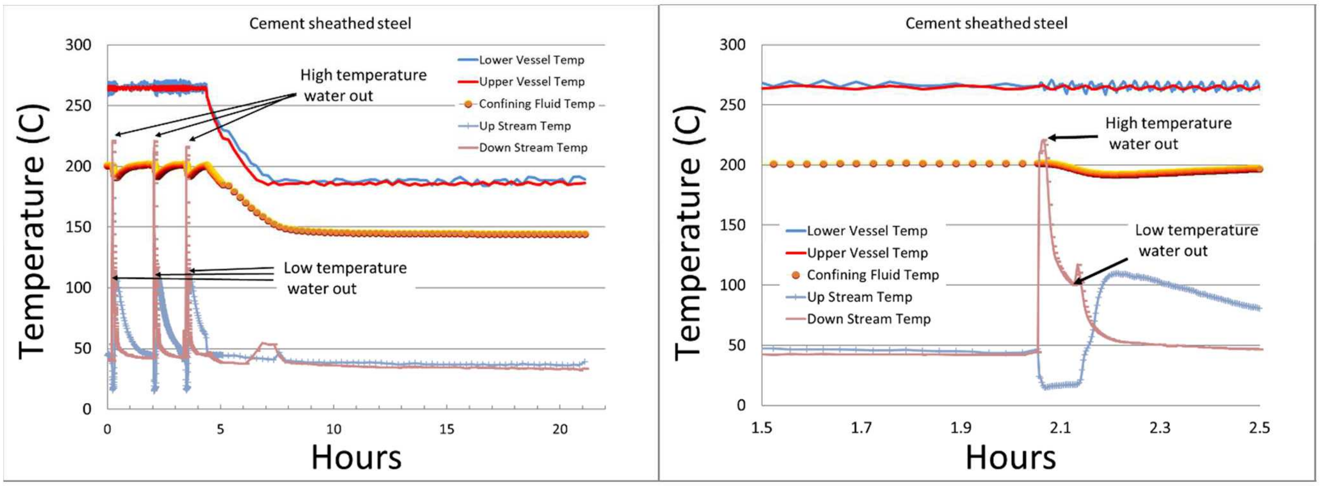

Figure 9. Test time versus temperature for components of the cement sheathed steel test (left). Test time versus temperature for components of the cement sheathed steel test with expanded time scale (right).

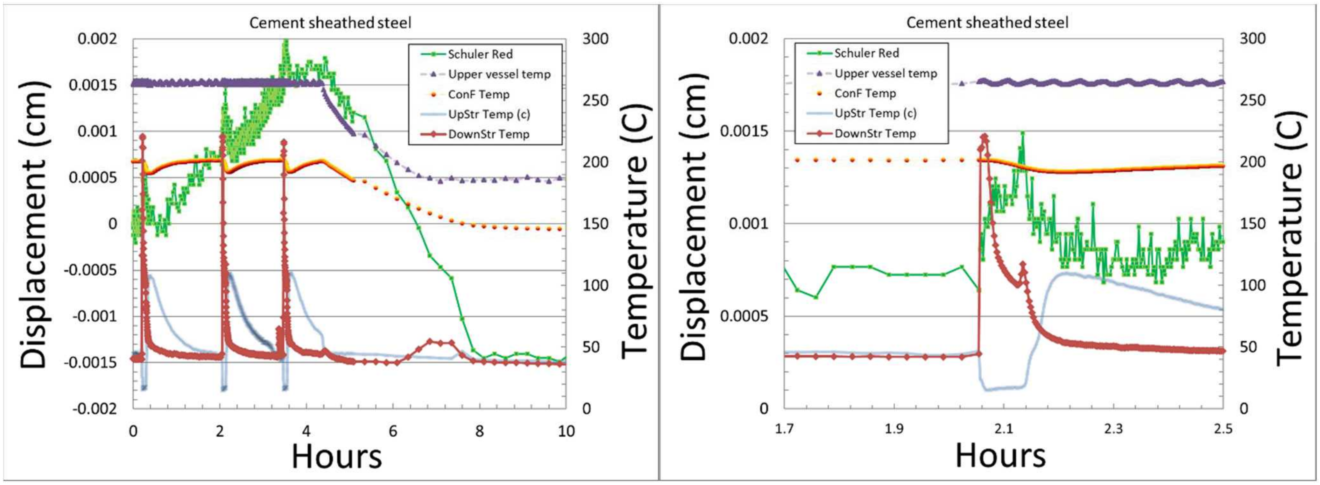

Figure 10. Test time versus sample displacement and temperature during flow periods for cement sheathed steel sample.

3.4 Observations

Observations of samples tested was limited to reflected light microscopy of sections cut through the samples. In Figure 11, viewing a slice parallel to the long axis, the cement sample looks unscathed by the hydrous thermal treatments. There are ever present round voids, occasionally the voids have white precipitate in them. At this scale, the sample looks relatively clean.

Shown in Figure 12 is the cement sheathed steel sample sliced perpendicular to the long axis. In it, there is a small fracture (red arrow) from the steel which extends to a round pore and non-round pores, perhaps suggesting that these pores were slightly deformed (from round) during the thermal cycling. It appears that the steel is well adhered to the cement from our observations and this warrants a closer look.

Figure 11. Cement sample sliced parallel to the long axis, reflected light.

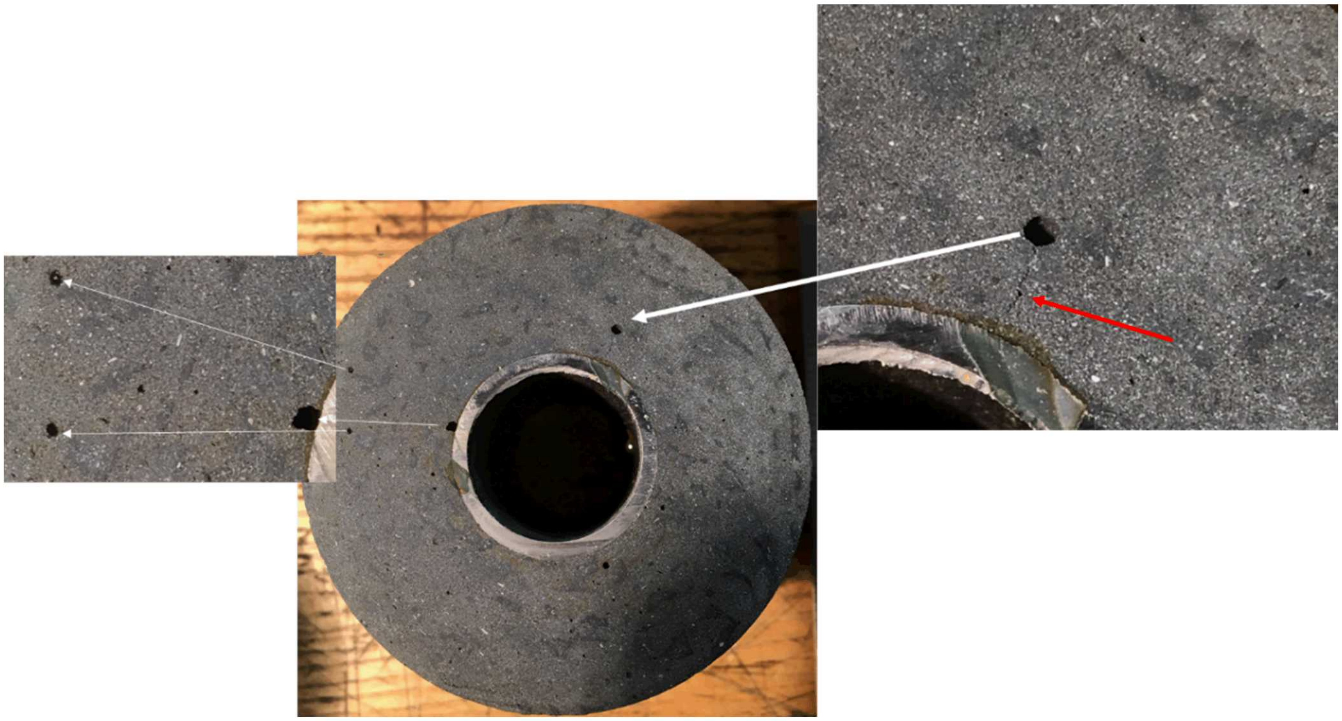

Figure 12. Cement sheathed steel sample sliced perpendicular to the long axis, reflected light.

3.5 Dry thermal shock

3.5.1 Sample appearance

Figure 13 shows changes in the appearances of the reference cement OPC/SiO_2 and TSRC sheath samples after the thermal cycling. The passage of cold water through the casing with OPC/SiO_2 sheath was accompanied by a bursting sound and formation of wide cracks in the composite sheath during the first cycle. The cracks were going through the whole length of the sheath and widened in 20 cycles. The color of the samples changed from grey to red because of the carbon steel corrosion under the cement sheath. This clearly indicated that cement did not protect the casing anymore.

TSRC, on the other hand, survived 9 cycles before thin cracks formed in the 10th cooling cycle. The cracks formed on the edges of the samples and did not continue through its entire length. These cracks propagated further along cement sheaths in 20 cycles. The color of the cement did not change except for some red spots at the top and bottom of the samples where CS tubes were open to the hydrothermal curing environment.

The final appearance of the samples and the interface between the tested cement composites and CS tube are shown in Figure 14. The difference in colors of the outside sheath layer reflects the conditions of the interface for OPC/SiO_2 and TSRC samples. The metal under the OPC/SiO_2 sheath corroded, scaling off from the tube and coloring the cement sheath itself. There was no cement attached to the tube. In the case of TSRC the casing was partially covered with the protective cement layer and corrosion spots appeared with metal scale in some locations. There were no cracks in bulk samples of TSRC and OPC/SiO_2 composites confirming the cement-casing interface being the weak point. The result was similar (not shown) for TSRC samples heated directly to 250°C after the initial curing (fast heating regime). Thin cracks formed at the edges of the cement sheath after the first 10 thermal cycles and corrosion spots were not detected at the interface at this point.

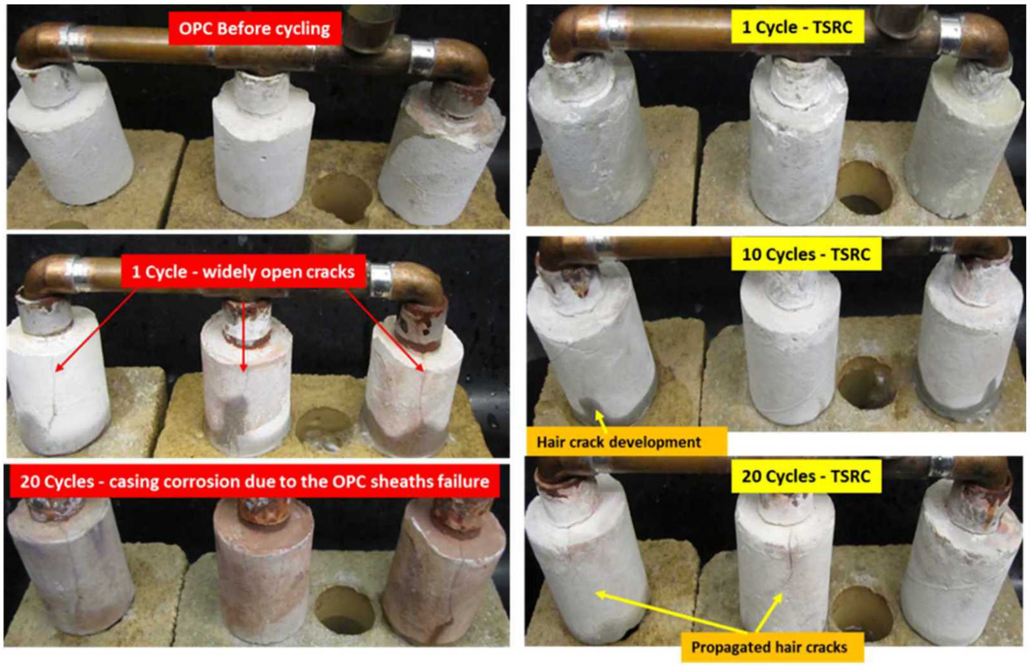

Figure 13. Changes in the appearance of OPC/SiO_2 (left) and TSRC (right) sheath samples during the thermal cycling (one cycle: 250°C dry heat → cold water through the casing → 250°C hydrothermal curing).

Figure 14. Appearance of OPC/SiO$_2$ sheath samples (top) and TSRC sheath samples (bottom) after 20 thermal cycles.

3.5.2 Mechanical properties

Tables 3 and 4 give results of the mechanical properties measurements for the TSRC samples before and after 20 thermal cycles (moderate initial temperature increase rate) or 10 thermal cycles (fast initial temperature increase rate). In both cases the compressive strength of the samples did not change significantly while the bond strength decreased. Interestingly the Youngs' modulus did not increase with the continuous cement curing and cycling. This is a positive feature since cements with lower Young's modulus are less susceptible to failure under common mechanical stresses during well operations [2]. The most significant difference for the two tested initial rates of temperature increase was lower sheath-shear bond strength and higher strength loss during the thermal cycling for the system cured under the fast temperature increase rate. The bond strength was nearly half of that for the system cured under the moderate rate of initial temperature increase and the bond loss was >30% in 10 cycles compared to 11% loss in 20 cycles for the TSRC samples subjected to the moderate initial temperature increase rate. As was mentioned earlier the heating of the well is unlikely to go as fast as we tested in our experiments, nevertheless this parameter may have to be taken into consideration during well operations – slow well-temperature increase or well cooling and allowing an additional time before the start of the operations may significantly help preserving the well integrity.

Table 5 shows results of the mechanical tests for OPC/SiO$_2$ blend. The initial compressive strength of this blend was more than double that of TSRC while the bond strength was similar (for the similar moderate rate of the initial temperature increase). This unusually high bond strength for the OPC/SiO$_2$ blend is due to the presence of micro-carbon fibers in the formulation. Hydration of this composite was faster resulting in faster strength build up and higher Young's modulus indicative of a more brittle material [6]. Both compressive strength and modulus did not change much during the cycling; however, the bond strength decreased dramatically by 84%. These data agree with the visual observations of crack formation in OPC/SiO$_2$ sheath samples and strong samples corrosion because of the poor protection of the carbon steel by the de-bonded cement sheath.

Table 3. Mechanical properties of bulk and sheath TSRC samples before and after 20 thermal cycles with moderate rate of the initial temperature increase

Number of cycles	Compressive strength, psi	Young's modulus, psi	Sheath-shear bond strength, psi
0	2030 ± 90	200110 ± 26810	180 ± 6
20	2085 ± 170	190990 ± 59820	160 ± 10

Table 4. Mechanical properties of bulk and sheath TSRC samples before and after 10 thermal cycles with fast rate of the initial temperature increase

Number of cycles	Compressive strength, psi	Young's modulus, psi	Sheath-shear bond strength, psi
0	2040 ± 120	217270 ± 11270	95 ± 6
10	1950 ± 110	181250 ± 19600	65 ± 11

Table 5. Mechanical properties of bulk and sheath OPC/SiO_2 samples for moderate rate of the initial temperature increase

Number of cycles	Compressive strength, psi	Young's modulus, psi	Sheath-shear bond strength, psi
0	4540 ± 200	384200 ± 41500	150 ± 10
10	3840 ± 210	358400 ± 46500	24 ± 6

3.5.3 Dimensional changes

Figure 15 shows changes in dimensions of TSRC and OPC samples during the thermal cycling. The behavior of the two composites is different – the TSRC sample expands slightly and the OPC/SiO_2 sample's dimensions do not change significantly during the cycles. The expansion could be due to the formation of new phases, phase transitions and carbonation of the sample during the heat exposure. Slow fly ash F reactions may contribute to gradual phase changes and formation of new phases leading to the sample expansion over the test period. The changes in OPC happen over a short time-period with faster hydrates crystallization and reactions with silica. Carbonation of the OPC samples during the heating did not seem to change the dimensions of the sample.

Shrinkage is one of the reasons of poor cement-casing bonding, so the slightly expansive nature that TSRC demonstrated in the cycling tests is favorable for the interfacial bonding in agreement with the mechanical tests that showed bond failure for OPC/SiO_2 sheath samples and a relatively small bond strength decline for TSRC sheath samples.

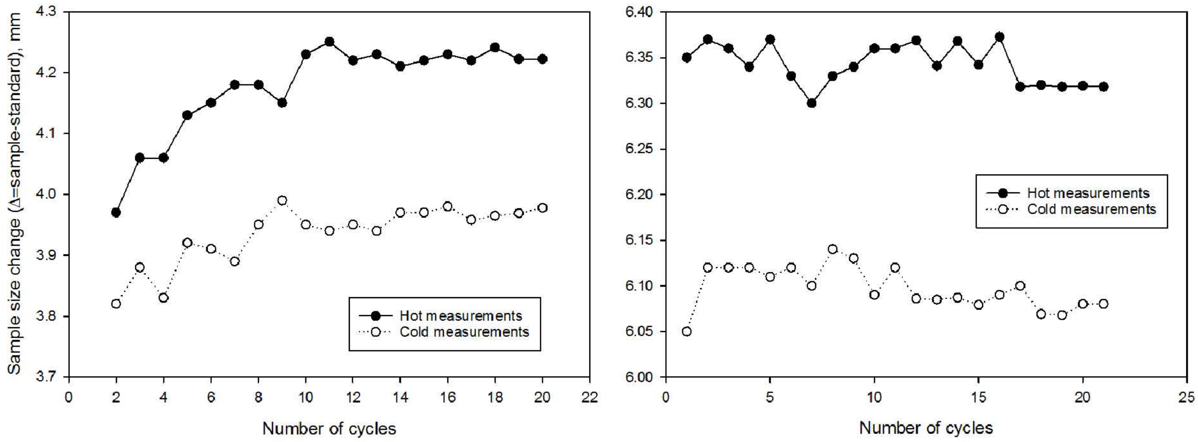

Figure 15. Sample size changes (difference between the cement sample and the standard bar) over the cycling period for TSRC (left) and OPC (right) in thermal cycling.

3.5.4 Coefficients of thermal expansion (CTE)

The changes in CTE in thermally stressed cements were similar for both TSRC and OPC/SiO_2 samples: the CTE dropped in the first cycles and then stabilized, the further changes were moderate especially in the case of the OPC-based formulation (Figure 16). For TSRC the coefficient slightly increased during the 20 severe cycles after the initial drop. For comparison, the CTE of steel remains constant in the thermal cycling (Figure 16) while the CTEs of both composites decrease. This increased the difference between composites' CTEs and the CTE of steel; however, the change was not dramatic and cannot account for the significant difference in the bond strength changes of the two tested composites. CTE changes at longer testing times could be more significant further affecting the bond strength.

In summary, the CTE change in the first cycle was the most significant while further changes were minor. Such a decrease in the CTE occurred while the composite was still reacting and forming new cementitious phases both in the matrix and at the interface with accompanied changes in mechanical properties. However, continuous composite reactions did not further decrease the CTE but stabilized it within the experimental conditions of 20 dry heat-cold water cycles. TSRC and OPC-based composites had similar trends of CTE changes over the test periods, so these changes cannot account for the dramatic difference in the bond strength and corrosion protection behavior of these composites.

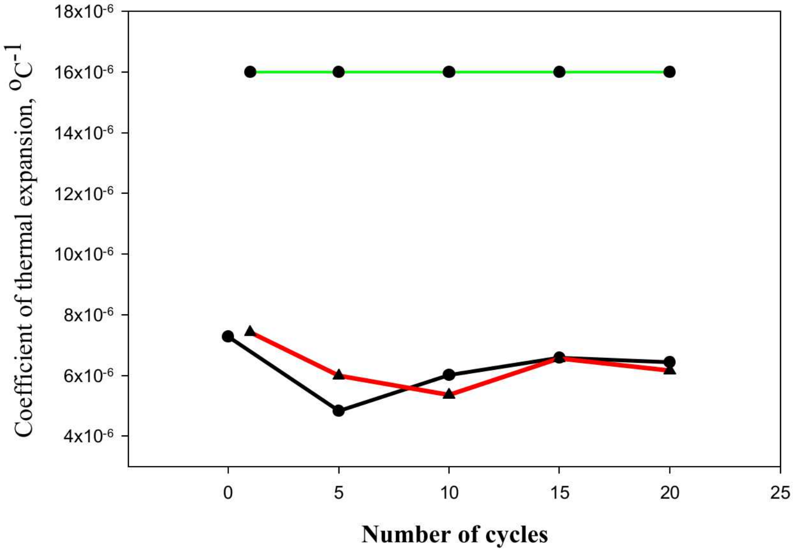

Figure 16. CTE of carbon steel (green), TSRC (black) and OPC (red) exposed to thermal cycling.

3.5.5 Crystalline composition (XRD) - TSRC

Figure 17 shows XRD patterns of TSRC samples before (red) and after (blue) 20 thermal cycles. For the matrix the major changes that occurred during the cycling included 1) disappearance or decrease in the intensities of the starting materials (e.g. sillimanite from fly ash F (ICDD: 04-007-8854), 2) low-silicon phases such as luicite (ICDD: 01-076-8733/00-038-1423) and sodalite (ICDD: 01-070-5028) were replaced by calcium-aluminum silicate dmisteinbergite (ICDD: 04-011-5220) that becomes the major crystalline reaction phase along with crystallization of silica (ICDD: 01-077-8639), and 3) there was increased sample carbonation, with formation of cancrinite group silicon-rich mineral cancrisilite (ICDD: 04-020-1220) and clearly increased peak of calcite (ICDD: 04-002-9082).

For the interface there was a couple of striking changes after the cycling in addition to the disappearance of the FAF peaks: 1) zeolite, analcime, detected in the interface control sample after the cycling was replaced by the carbonated cancrinite group mineral cancrisilite (ICDD: 04-020-1220), 2) feldspar mineral, dmisteinbergite (ICDD: 04-011-5220), predominant in the matrix was also detected at the interface, and 3) the calcite peak was even stronger at the interface than in the matrix.

In summary, the cycling resulted in further reactions of FAF with release of additional silicon that assisted in formation of silicon-rich phases both at the interface and in the matrix. It also produced carbonation of the composite with formation of desirable dense cancrinite group mineral phase (cancrisilite) and undesirable calcite phase, especially at the interface, where large calcite crystals negatively affect the bond strength.

3.5.6 Amorphous and crystalline compositions (FTIR) – TSRC

Figure 18 shows FTIR spectra of TSRC samples before and after 10 or 20 thermal cycles. Comparison of the spectra clearly shows increased crystallinity of the samples during the cycling: the ratio of absorbance peaks between crystalline and amorphous calcium/sodium-aluminum-silicate (898cm^{-1}/994cm^{-1}) increases unambiguously. Compared to the control, the ratio increases by 2.4 times for the matrix and by more than 9 times for the interface. Such rise of the interface crystallinity increases vulnerability of the composite-metal bond. In agreement with the XRD results there is an increase in carbonated hydrates (1514 and 1403cm^{-1}), silica (11.76 cm^{-1}) and crystalline aluminum-silicate hydrates (675 cm^{-1}). There is also a clear intensification of the silica gel peak both at the interface and in the matrix due to the further decomposition of FAF. This phase is a source of silicon for further crystallization of silica and silicon-rich phases detected by XRD. The interface has a growing amount of aluminum oxide hydroxide, which agrees with the XRD findings of the TSRC samples after 10-cycles (not shown).

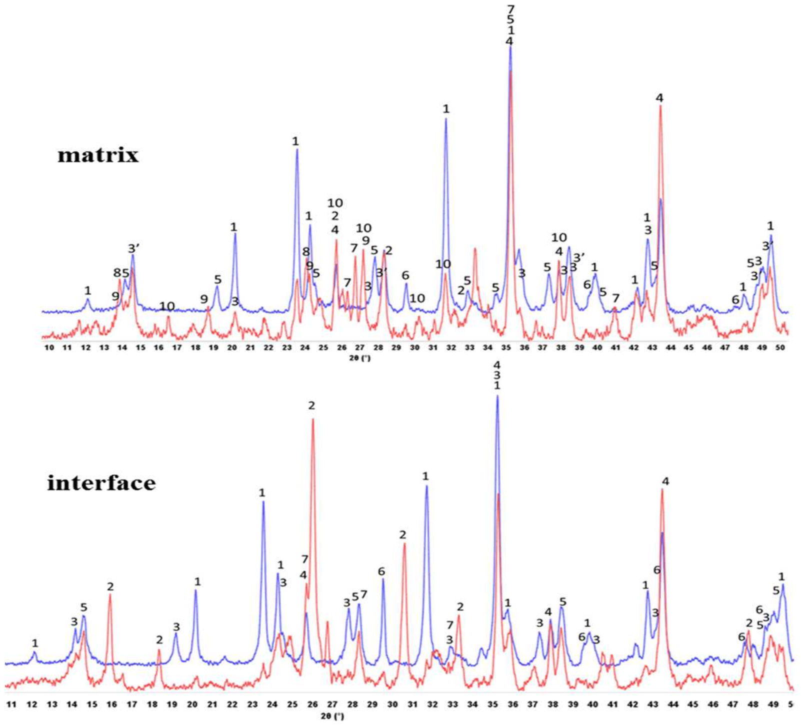

Figure 17. XRD patterns of matrix and interface of TSRC before (red) and after (blue) 20 thermal cycles. Matrix: 1-dmisteinbergite, 2-silica, 3-tohdite, 4-corundum, 5-cacrisilite, 6-calcite, 7-sillimanite, 8-sodalite, 9-hydroxycancrinite, 10-luicite Interface: 1-dmisteinbergite, 2-analcime, 3-cancrisilite, 4-corundum, 5-boehmite, 6-calcite, 7-silica

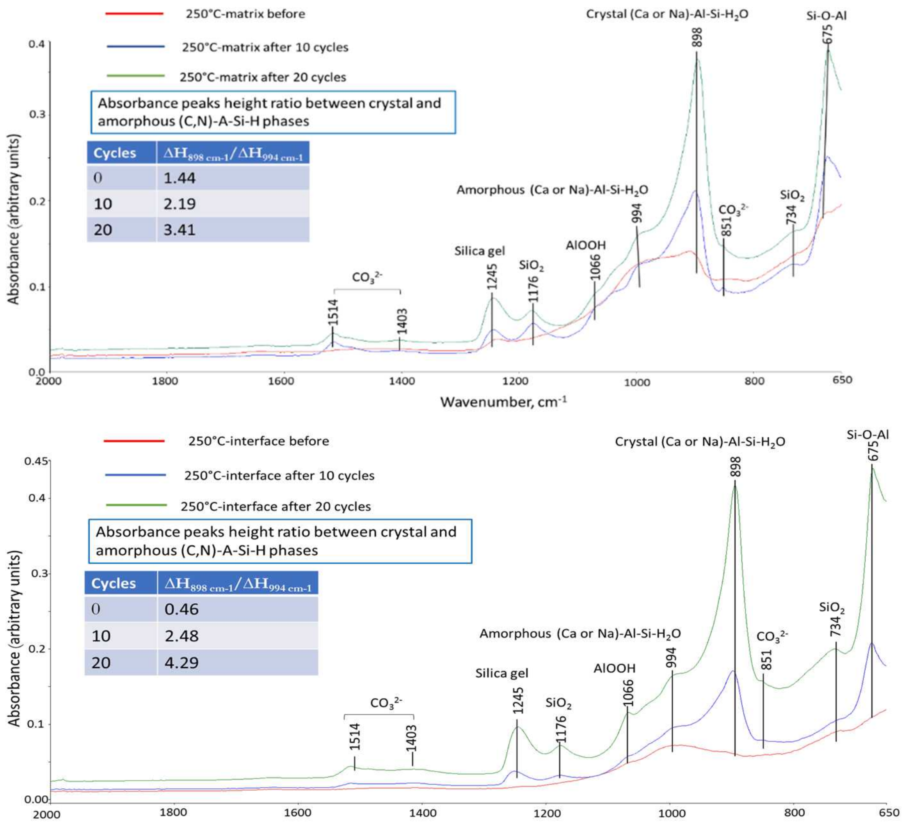

Figure 18. FTIR spectra of TSRC matrix and interface samples before and after thermal cycles.

3.5.7 Morphology and elemental analyses (SEM/EDX) – TSRC

Figures 19 and 20 show typical TSRC matrix and interface microstructures and elemental compositions. (Note that the silver signal visible on all the photomicrographs is from the silver coating used to eliminate charging effects during the measurements.) After 20 thermal cycles TSRC matrix was for the most part amorphous (Figure 19). There were non- or partially-reacted FAF particles and carbon fibers imbedded into the matrix. The elemental composition of the matrix was aluminum-rich calcium-aluminum silicate hydrates. Small platelet-like structures, imbedded into the amorphous matrix, had elemental composition of dmisteinbergite identified by XRD. This hydrate presented dense features often seen in large circular arrangements in the matrix.

Figure 20 shows two photomicrographs of the TSRC interface after 20 cycles. As for the matrix it was for the most part amorphous with some defined features. The spots with no clear features were rich in aluminum (Figure 20). Those with some platelet-like structure had elemental composition of dmisteinbergite or cancrisilite. Iron was also measured in the platelets possibly because of the incorporation of the tetrahedral iron into the structure of the cancrisilite, reported earlier for cancrinite [7]. The two possible sources of iron are FAF and the steel. Since iron was detected at the interface but not in the matrix steel was its likely source. Such interactions could help improve interfacial bond strength. Carbon was difficult to identify unambiguously because of the carbon fibers distributed throughout the matrix. The layer next to the interfacial one had better-visible features of separate platelets grown in different directions and tightly interconnected. The bigger crystals of 10-30 µm in size had elemental composition of calcium carbonate. These big crystals are unfavorable for the integrity of the interfacial layer and the bond strength.

In summary, morphological analyses showed for the most part amorphous structure at the interface rich in aluminum. Some interfacial phases with platelet-like structures included iron from carbon steel into their structures possibly improving the bonding. Presence of partially reacted FAF particles suggests that TSRC still has healing capacity after 20 thermal cycles.

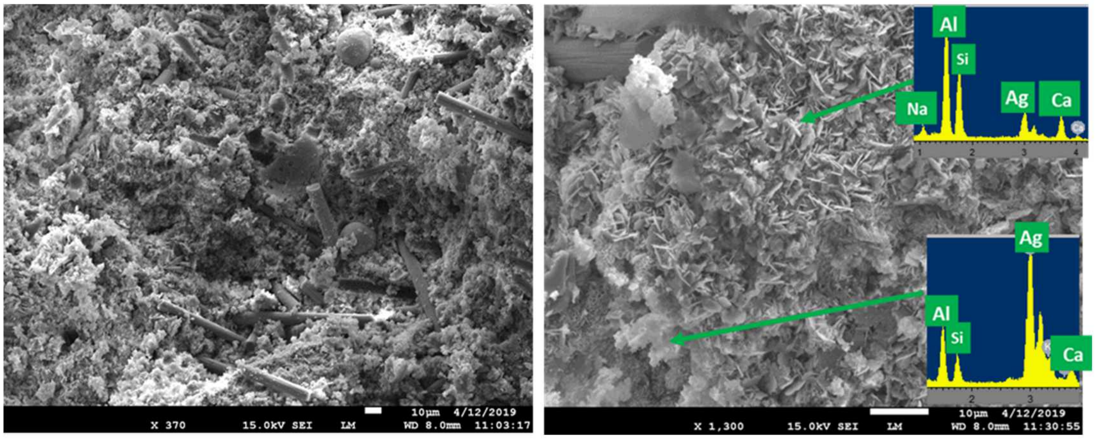

Figure 19: Scanning electron photomicrographs and elemental composition of typical TSRC matrix microstructures after 20 thermal cycles.

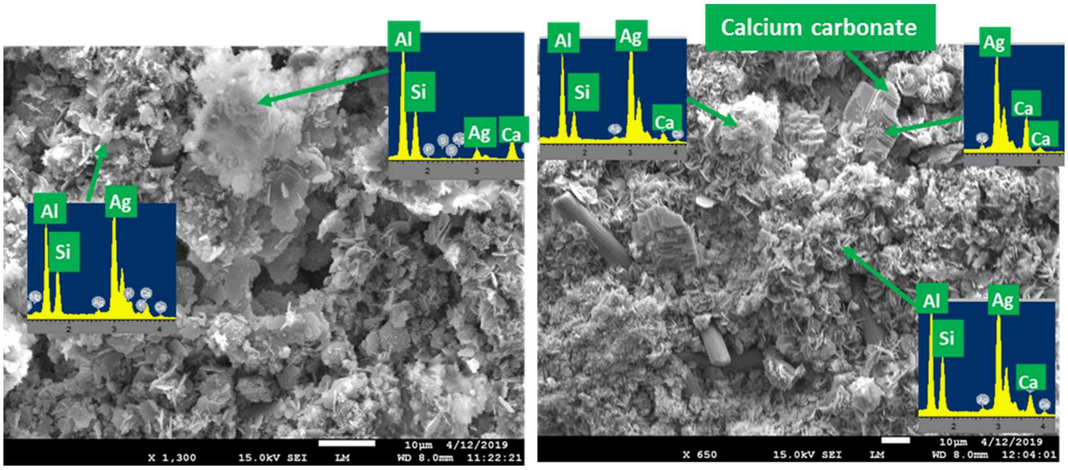

Figure 20: Scanning electron photomicrographs and elemental composition of typical TSRC interface microstructures after 20 thermal cycles (left-metal side; right – cement side).

3.5.8 Crystalline composition (XRD) – OPC/SiO$_2$

Figure 21 shows XRD patterns of OPC/SiO$_2$ samples before (red) and after (blue) 20 thermal cycles. Unlike for TSRC the matrix pattern of the treated samples was very similar to that of the control. The major crystalline phase was high-temperature calcium-silicate hydrate, xonotlite (ICDD: 00-023-0125). The major difference was appearance of the hydration products of the cement interstitial phase (C$_4$AF). The decrease in the shoulder at 2Θ ~12.42 is due to the hydration of this phase that forms such products as andradite (ICDD: 01-071-3855) and grossular hydroxylian (ICDD: 00-042-0570). There is also increase in the peak of calcium carbonate after the cycling.

For the interface the changes in the XRD patterns after the cycling were dramatic. The XRD pattern of the control interface sample was very similar to that of the matrix, dominated by xonotlite. After the cycling the xonotlite peaks disappeared; the new peaks on the pattern matched hematite (ICDD:04-006-0285) and iron oxide hydroxide patterns (ICDD: 01-084-6030). Iron oxides gave the rust coloring to the interface. Since the casing was completely detached from the cement, the interface sample was scraped from the cement itself and some of the cement hydrates contributed to the pattern (e.g. andradite and grossular present in the matrix). Additionally, iron and aluminum-containing phases formed at the interface, including calcium-aluminum-iron oxide (ICDD: 04-015-8014), srebrodolskite, aluminian (ICDD: 04-014-66-34) and grossular ferroan (ICDD: 01-082-9677). The patterns of the latter two phases strongly overlap with the first one and are not marked on the figure. There were also peaks of iron-calcium oxide, harmunite and calcium carbonate.

In summary, the crystalline composition of the OPC/SiO$_2$ is stabilized after the initial high-temperature curing with xonotlite being the predominant phase in the matrix. Only minor changes due to the further reactions of the calcium-iron-aluminate interstitial phase take place during the cycling in the matrix. On the other hand, xonotlite is not stable at the interface – it decomposes, and casing corrosion and decomposition-cement-reaction products replace xonotlite. Iron from corroded metal forms new calcium-aluminum-silica-iron oxides. These products are unfavorable for the interfacial bonding. Noticeably, there are aluminum-containing hydrates predominantly present at the interface even for this formulation with low aluminum content.

3.5.9 Amorphous and crystalline compositions (FTIR) – OPC/SiO$_2$

Figure 22 shows FTIR spectra of OPC/SiO$_2$ samples before and after 20 thermal cycles. The spectra of the matrix before and after the cycling resembled each other. The features of the spectrum after the cycling were not as well resolved as on the spectrum before it but all major peaks were present. The interface spectra before and after the cycling differed significantly in three major ways: 1) the major peak of calcium-silicate bonding at 968 cm^{-1} decreased drastically while there appeared the peak at 1005 cm^{-1} corresponding to the Fe-O-Si linkage in calcium-aluminum-iron-silica hydrates suggested by XRD analyses, 2) there was a noticeable increase in carbonation (peaks at 1489 and 1453 cm^{-1} and a peak at 877 cm^{-1}) and 3) increase in silica gel peak at 1200 cm^{-1}. The decreased intensity of the peak of calcium-silicate hydrate, increased carbonate and silica gel peaks suggest decomposition of crystalline calcium silicates with formation of calcium carbonate and release of silica gel that partially crystallizes into quartz (peak at 669 cm^{-1}). This carbonation process destroys cement at the interface and is of concern for geothermal environments that are generally CO$_2$-rich.

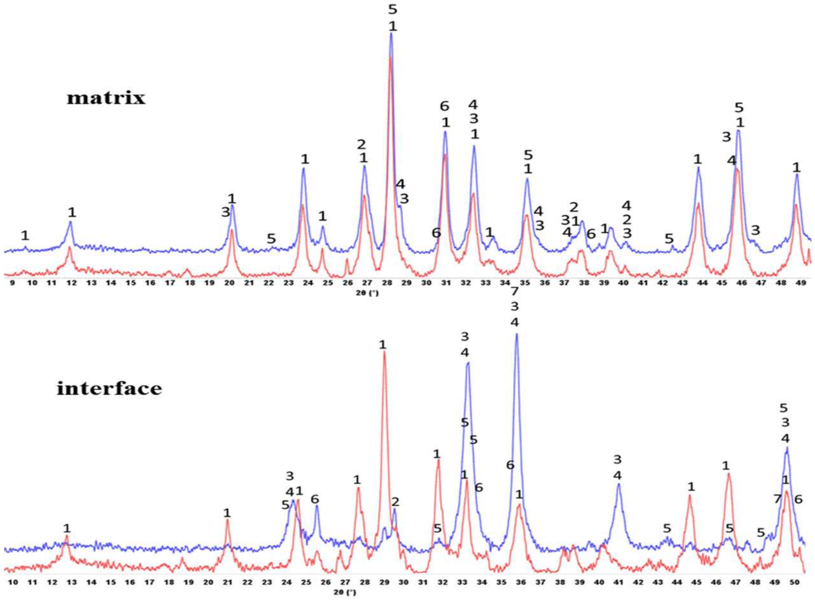

Figure 21. XRD patterns of matrix and interface of OPC/SiO$_2$ blend before (red) and after (blue) 20 thermal cycles.
Matrix: 1-xonotlite, 2-silica, 3-andradite, 4-grossular hydroxylian, 5-calcium carbonate, 6-calcium hydroxide.
Interface: 1-xonotlite, 2-silica, 3, 4- iron oxide hydroxide and hematite, 5-calcium-aluminum-iron oxides and hydroxides, 6-iron-calcium oxide (harmunite), 7-carbonate

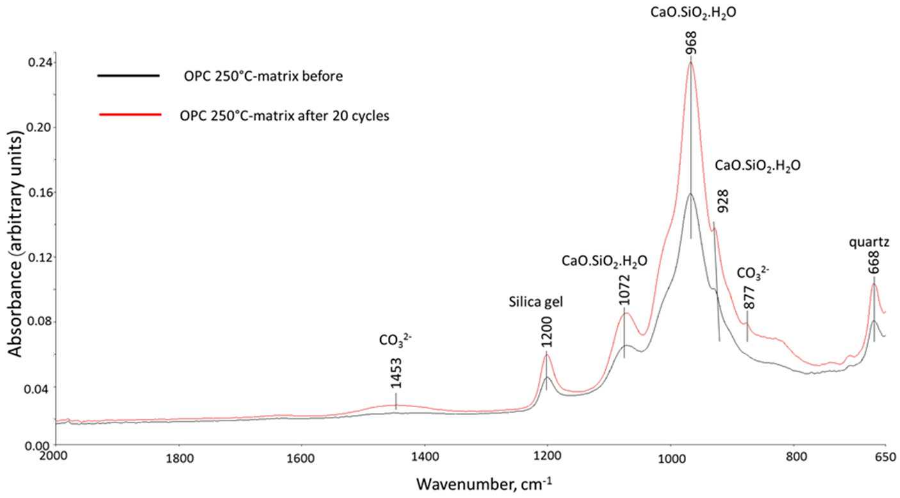

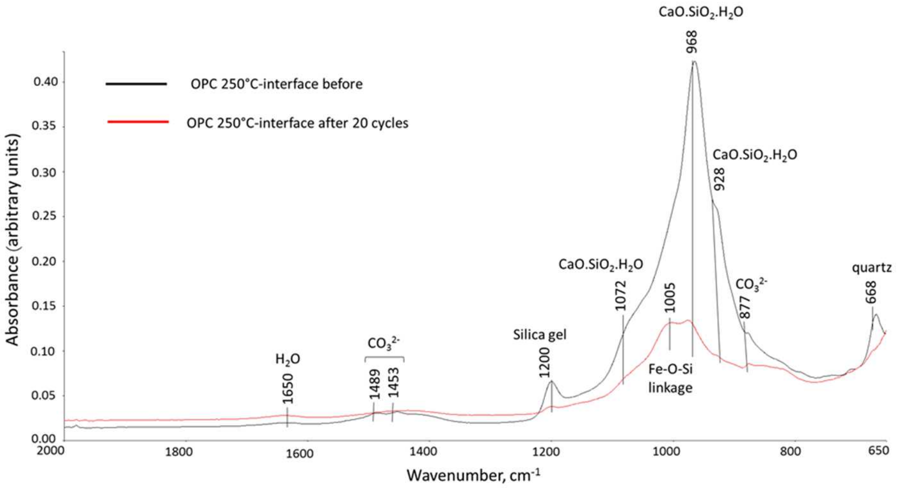

Figure 22. FTIR spectra of OPC/SiO$_2$ matrix and interface samples before and after 20 thermal cycles.

3.5.10 Morphologies and elemental analyses (SEM/EDX) – OPC/SiO$_2$

Figures 23 and 24 show typical OPC/SiO$_2$ matrix and interface microstructures and elemental compositions, respectively. After 20 thermal cycles the composite matrix was dense with inclusion of holes (Figure 23). These holes were filled with small calcium-silicate crystals (~1 μM; Ca:Si = 4:5) and deposits of big calcium carbonate crystals. Crystals in the shape of long needles had typical elemental composition of xonotlite. Significant parts of the matrix were still amorphous and silicon-rich.

Figure 24 shows photomicrographs of OPC/SiO$_2$ interface with carbon steel. The interface presented almost a powder-like crumbling amorphous product with granular-morphology for the most part, rich in silicon and iron in agreement with the FTIR findings of –Fe-O-Si- linkage. Some parts of the interface were fluffy-amorphous (top) and in addition to silicon and iron had aluminum and magnesium in their composition. Underneath this amorphous layer that was in contact with the steel there appeared tiny calcium-aluminate crystals. It is remarkable that for Ca-rich blend of OPC/SiO$_2$ there was no or little calcium in contact with the steel. Another remarkable feature was composite interactions with the carbon fibers: the fibers were covered with the silicon-iron amorphous composite hydrates that reacted with the fibers surface. For comparison the carbon fibers in the matrix were completely free of the cement – unlike iron-silicates, calcium-silicate hydrates did not interact with the carbon fibers. These observations suggest poor Ca interactions with carbon steel and fiber surfaces.

The microstructural studies demonstrated the following clear differences in compositions of TSRC and OPC/SiO$_2$ composites: 1) TSRC matrix underwent compositional changes during 20 thermal cycles, these are mostly due to the slow reactions of FAF and carbonation with formation of high-temperature stable carbonated calcium-aluminum silicates. OPC/SiO$_2$ matrix composition did not change significantly in 20 thermal cycles, calcium-silicates formed after the first day of high-temperature curing remained the major phases after the cycling. 2) The morphologies and compositions of TSRC matrix and interface were very similar. Composition of the OPC/SiO_2 composite interface drastically changed during the cycling – the originally formed hydrates were replaced by amorphous iron-aluminum-silicates, silica gel and calcium carbonates disconnected from the matrix and metal surfaces.

The difference in the interfacial interactions of TSRC and OPC/SiO_2 composites could be explained by the differences in their chemistries. Highly alkaline slurries of both composites form a protective layer at carbon steel casing, however the further interactions differ. In the case of TSRC readily available sodium metasilicate ($Na^+OSi(OH)_3^-$) reacts both with $Al(OH)_4^-$ from calcium aluminate cement and with the metal surface protective layer (Fe-OH) to form NaOH and Fe-O-Si linkage further stabilized by the Al into iron substituted (Na)-silicon-aluminum-hydrates that later transfer to stable carbonates (cancrinite and cancrisilite). The EDX measurements suggested inclusion of iron into the cancrisilite/cancrinite network, possibility of which was reported earlier [7]. Slowly reacting TSRC blend components, form predominantly amorphous phases at the interface, which can accommodate the new phases into the cement matrix. Below are schematics of possible formation pathways of interfacial TSRC phases.

$Na^+OSi(OH)_3^-$+ Fe-OH (protective layer) + $Al(OH)_4^-$ + H_2O $\rightarrow$ NaOH + Na_2O-SiO_2-(Al_2O_3,Fe_2O_3)-H_2O (amorphous) + CO_2 $\rightarrow$ cancrinite/cancrisilite ($Na_7(Al_5Si_7O_{24})$ $(Fe_2O_3)(CO_3)(H_2O)_3$) (solid crystalline) + Na_2CO_3

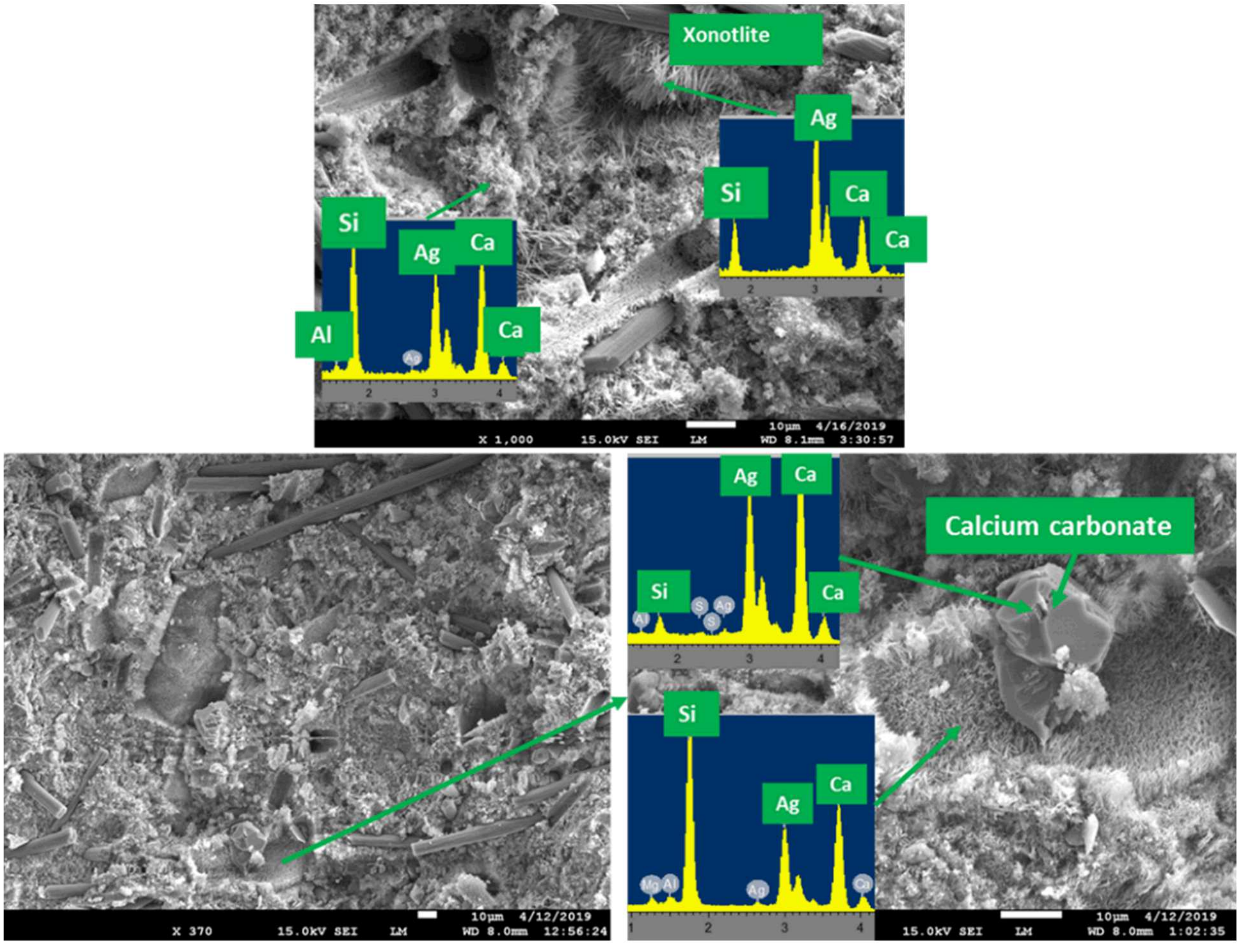

Figure 23. Scanning electron photomicrographs and elemental composition of typical OPC/SiO_2 matrix microstructures after 20 thermal cycles.

For the OPC/SiO_2 blend the Fe-OH also forms amorphous products with Fe-O-Si linkages at the interface. However, these are not included into a stable (Na)-aluminum-silicate network. The fast-reacting OPC/SiO_2 blend forms rigid interfacial phases shortly after the start of the hydration reactions, so the newly formed iron-containing interfacial products are of a larger volume than the original protective layer on the steel and produce a stress at the rigid interfacial layer that cannot accommodate the changes. After longer testing times, these amorphous products with Fe-O-Si linkage destroy the casing protective layer completely, by detaching from the cement sheath and spalling, and scaling off the surface of the casing as rust leaving it unprotected from corrosion.

Along with the carbonation of the interface these scale-forming products destroy the cement-metal bond. The chemistry of the cement matrix does not have any capability to recover this bonding.

In the case of TSRC, the bond is partially destroyed with the formation of calcium carbonate. After 20 thermal cycles the cement has capacity to recover the bond, at least partially, through slow pozzolanic reactions of non-reacted FAF particles remaining in the cement.

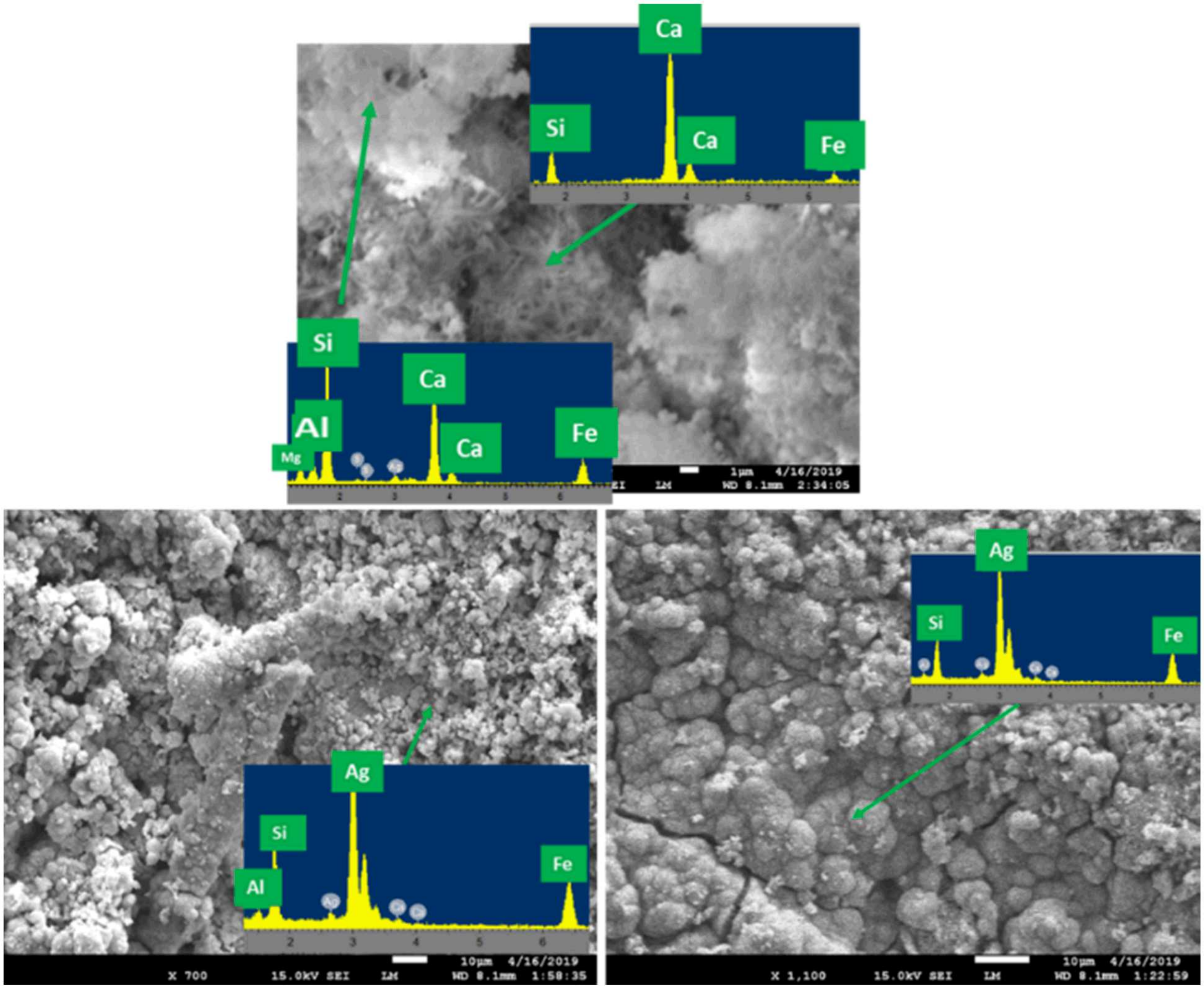

Figure 24: Scanning electron photomicrographs and elemental composition of typical OPC/SiO_2 interface microstructures after 20 thermal cycles.

4 CONCLUSIONS

This paper documents additional evaluations of Thermal Shock-Resistant Cement (TSRC) developed by Brookhaven National Laboratory (BNL). The work focused on thermal expansion, and fluid flow through the TSRC, and the application of thermal shock to a steel/TSRC sheathed sample.

The key contributions of this work to the geothermal community are centered about development of a test system to make measurements of cement thermal expansion and fluid flow at elevated temperature (up to 200°C) and confining pressure (13.8 MPa) pressure and pore water pressure (10.3 MPa) relevant to geothermal systems.

The thermal expansion coefficient of the water-saturated TSRC is in the range of 1 to 5 x 10^{-5}/°C, over this temperature range at 3.5 MPa effective confining pressure, and the estimated permeability of the TSRC may be temperature dependent and is on the order of 0.1µD.

The test system, modified to thermally shock a steel/TSRC sheathed sample at elevated temperature and pressure conditions, successfully created a 100°C radial thermal gradient in about five minutes. Some thermally induced cracking may be present.

Comparison of TSRC and OPC-based formulation demonstrated that the common high-temperature well cement cannot provide long-term integrity of high-temperature storage wells under severe thermal stresses (dry-heat-cold water thermal shock conditions). The interfacial cement-metal bond fails first, followed by casing corrosion and failure. In the conducted tests the cement sheath broke in the first cycle forming wide continuous cracks and lost 84% of the bond strength after 20 cycles and compromised carbon steel corrosion protection.

Advanced TSRC performed significantly better under similar conditions: it lost 11% of its bond strength in 20 cycles and for the most part provided continuous protection of the casing from corrosion. However, TSRC formed thin non-continuous cracks that resulted in some CS corrosion after 20 severe TS cycles.

The CTE changes in severe TS cycles were similar for both TSRC and OPC and unlike reported by other authors [8] could not account for the changes in mechanical properties of the interfacial bond, cement sheath damage and steel corrosion under the test conditions.

Phase change analyses demonstrated preferential formation of aluminum-rich phases at the interface and growing crystallinity of TSRC samples, accompanied by the decrease in the bond strength suggesting importance of amorphous aluminum-rich phases for the strong interfacial bonding.

5 ACKNOWLEDGEMENTS

We graciously acknowledge the Geothermal Technologies Office for supporting this research and specifically Arlene Anderson. Sandia National Laboratories is a multimission laboratory managed and operated by National Technology and Engineering Solutions of Sandia, LLC., a wholly owned subsidiary of Honeywell International, Inc., for the U.S. Department of Energy's National Nuclear Security Administration under contract DENA0003525.

6 REFERENCES

1. Sugama, T. & Pyatina, T. *Alkali-activated cement composites for high temperature geothermal wells*. (Scientific Research Publishing, Inc., 2017).

2. Sugama, T. & Pyatina, T. Self-Healing , Re-adhering , and Corrosion-Mitigating Inorganic Cement Composites for Geothermal Wells at 270-300C. *BNL-211405-2019-INRE* (2019).

3. Pyatina, T. & Sugama, T. Toughness improvement of geothermal well cement at up to 300oC: Using carbon microfiber. *J. Compos. Mater.* **4**, 177–190 (2014).

4. Schuler, K. W. Lateral-deformation gage for rock-mechanics testing. *Exp. Mech.* **2449**, 15–18 (1996).

5. Pyatina, T. & Sugama, T. Cements for high-temperature geothermal wells. in *Cement based materials* (eds. Saleh, H. & Abdel Rahman, R. O.) 221–235 (2018).

6. Sugama, T. & Pyatina, T. Self-healing, re-adhering, and corrosion-mitigating inorganic cement composites for geothermal wells at 270-300degC. *BNL-2019-IR* (2019).

7. Latham, K., Williams, C. D. & Duke, C. V. A. The synthesis of iron cancrinite using tetrahedral iron species. **2449**, 15–18 (1996).

8. Bu, Y., Chang, Z., Du, J. & Liu, D. Experimental study on the thermal expansion property and mechanical performance of oil well cement with carbonaceous admixtures. *RSC Adv.* **7**, 29240–29254 (2017).